

## Supporting Information

# Suspensions of Semiconducting Nanoparticles in Nafion for Transient Spectroscopy and Terahertz Photoconductivity Measurements

Jacob A. Spies<sup>a</sup>, Miryl J. Hilibrand<sup>a</sup>, Jens Neu<sup>b</sup>, Sarah Ostresh<sup>a</sup>, John R. Swierk<sup>a,‡</sup>, Charles A. Schmuttenmaer<sup>a\*</sup>

<sup>a</sup>Department of Chemistry and Energy Sciences Institute, Yale University, New Haven, Connecticut 06520, United States

<sup>b</sup>Department of Molecular Biophysics and Biochemistry and Microbial Sciences Institute, Yale University, New Haven, Connecticut 06520, United States

<sup>‡</sup>Current Address: Department of Chemistry, State University of New York at Binghamton, Binghamton, NY 13902

### Table of Contents

<b>Additional Experimental Details</b> .....	S2
<i>Optimization of Nafion Film Deposition Procedure</i> .....	S2
<i>Terahertz Time-Domain Spectrometer</i> .....	S2
<i>Time-Resolved Terahertz Spectrometer</i> .....	S2
<b>Figure S1</b> .....	S3
<b>Table S1</b> .....	S3
<i>Numerical Photoconductivity Data Processing Procedure</i> .....	S4
<b>Figure S2</b> .....	S5
<b>Materials Characterization</b> .....	S6
<b>Figure S3</b> .....	S6
<b>Figure S4</b> .....	S6
<b>Table S2</b> .....	S6
<b>Supplemental Terahertz Results</b> .....	S7
<i>Optical-Pump Terahertz-Probe Measurements</i> .....	S7
<b>Figure S5</b> .....	S7
<b>Figure S6</b> .....	S7
<b>Figure S7</b> .....	S8
<b>Table S3</b> .....	S8
<i>Time-Resolved Terahertz Spectroscopy Measurements</i> .....	S8
<b>Figure S8</b> .....	S8
<b>Figure S9</b> .....	S9
<b>Table S4</b> .....	S9
<b>Figure S10</b> .....	S9
<b>Table S5</b> .....	S10
<b>Table S6</b> .....	S10
<i>Comparison of No Model and Thin Film Photoconductivity</i> .....	S11
<b>Figure S11</b> .....	S11
<b>References</b> .....	S11

## Additional Experimental Details

### *Optimization of Nafion Film Deposition Procedure*

To optimize film preparation for a larger scale, several iterations of the procedure in Reier et al.<sup>1</sup> (which drop-casts 10  $\mu\text{L}$  of Nafion ink onto an electrode) were tested. In Reier et al, thickness and sample uniformity present few issues due to the small scale ( $< 5$  mm in diameter, 10  $\mu\text{L}$  volume deposited). However, when using larger volumes that are needed to prepare films for THz spectroscopic measurements, sample thickness and uniformity can be problematic. Variations in volume ratios of Nafion to nanoparticle, deposition volume, and drying temperature were tested to optimize this procedure. Volume ratios of 1:1, 3:1, and 5:1 (Si:Nafion) were assayed, drying temperatures were varied from 40  $^{\circ}\text{C}$  to 80  $^{\circ}\text{C}$ , and single layer deposition volumes were varied from 100  $\mu\text{L}$  to 125  $\mu\text{L}$ . We found that 3:1 Si:Nafion films dried at 80  $^{\circ}\text{C}$  with 115  $\mu\text{L}$  per layer in 1  $\text{cm}^2$  wells yielded the most reproducibly uniform films. However, film uniformity under these parameters may vary with different materials. In particular, the size of the particles should guide procedural optimization.

The most crucial step in creating homogeneous multilayer films was the first deposition. It was important to avoid over-drying the sample during the first deposition ( $\approx 5$ -7 minutes drying time), as this caused significant wetting toward the edges of the well. Subsequent layer depositions stabilized the film, and produced a more homogenous sample. These additional layer depositions were typically dried for 5-10 minutes to reduce the sample volume in the well. After the last layer was deposited, the sample was dried for 10-20 minutes to yield the final film. We recommend depositing at least three layers (as used in the measurements for this work).

### *Terahertz Time-Domain Spectrometer*

THz time-domain spectroscopy (THz-TDS),<sup>2</sup> which is the steady-state THz technique used for materials characterization in this work, was performed using a home-built instrument as previously reported by our group.<sup>3,4</sup> The output of a Ti:Al<sub>2</sub>O<sub>3</sub> (Ti:Sapphire) oscillator (KMLabs Griffin, 800 nm center wavelength, 90 MHz repetition rate, 3.5 nJ pulse energy, 20 fs pulse duration) was split into two beams for THz generation and detection, respectively. THz radiation was generated and subsequently detected using two separate photoconductive antennae (Batop). The time-delay between THz generation and detection was controlled using a mechanical delay stage.

### *Time-Resolved Terahertz Spectrometer*

Time-resolved terahertz (THz) spectroscopy (TRTS) was performed using a home-built instrument as previously reported by our group.<sup>5-7</sup> The output of a Ti:Al<sub>2</sub>O<sub>3</sub> chirped-pulse regenerative amplifier (Spectra Physics Spitfire Ace, 800 nm center wavelength, 1 kHz repetition rate, 4 mJ pulse energy, 35 fs pulse duration) was split into three beams for THz generation, THz detection, and optical photoexcitation, respectively. THz radiation was generated in a two-color air plasma<sup>8,9</sup> and was subsequently detected via free-space electro-optical sampling in a ZnTe (110) crystal.<sup>10</sup> The optical photoexcitation beam was frequency-doubled to 400 nm in a  $\beta$ -barium borate (BBO) crystal and attenuated using a variable neutral density filter. The time delay between the optical pump and THz probe in addition to the THz probe and detection beam were controlled using two mechanical delay stages, respectively. A representative THz pulse is shown in Figure S1a.

Full TRTS measurements entail measuring the entire THz pulse at some particular time after photoexcitation. Then the full complex-valued frequency-dependent photoconductivity can be determined. On the other hand, it is often useful to simply monitor the largest amplitude point in the THz waveform (indicated with the green circle in Figure S1a) as a function of pump-probe delay time in order to measure the overall THz attenuation. This provides information on carrier generation dynamics and trapping dynamics, but not the full, frequency-resolved photoconductivity spectrum.

The pump (optical) and probe (THz) spot sizes were determined using knife-edge measurements. The results of the knife edge measurements were fit with Equation S1, where  $P(x)$  is the measured power or amplitude,  $p_0$  is the baseline offset,  $p_m$  is the maximum power or amplitude, “erf” is the error function,  $x$  is the knife position,  $x_0$  is the

beam center position, and  $w$  is the  $1/e^2$  beam radius. Figure S1b-c shows the results of the knife-edge measurements fit using Equation S1. The results from the fit are shown in Table S1.

$$P(x) = p_0 + \frac{p_m}{2} \left[ 1 - \operatorname{erf} \left( \sqrt{2} \frac{x - x_0}{w} \right) \right] \quad (\text{S1})$$

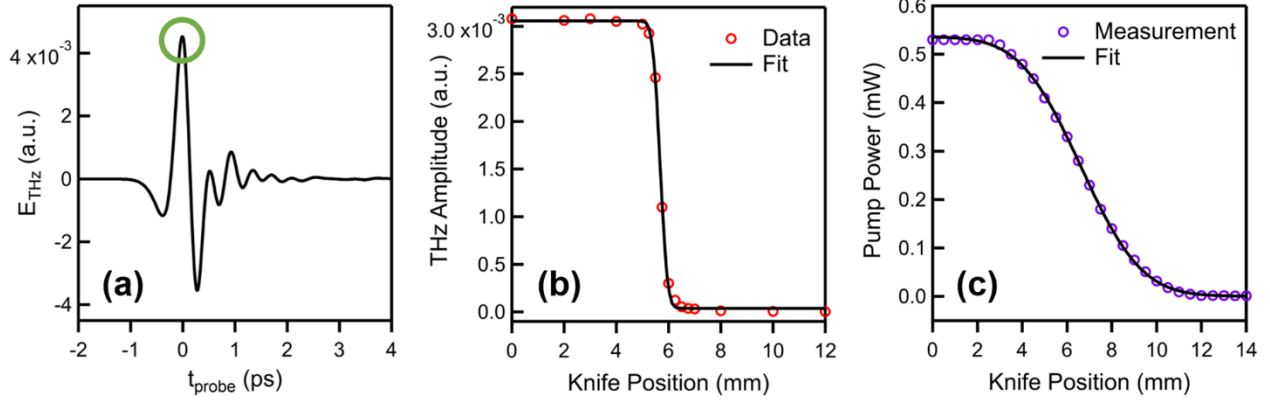


**Figure S1.** (a) Representative THz pulse. The green circle on the peak indicates the point at which difference measurements are made in optical-pump THz-probe measurements. (b) Knife-edge measurement and fits using Equation S1 for the THz probe beam. (c) Knife-edge measurement and fits using Equation S1 for the optical excitation beam at 400 nm.

**Table S1.** Fit parameters for knife edge measurements of the THz probe beam and optical pump beam at 400 nm. Reported errors are fitting uncertainties.

Parameter	THz Probe	Optical Pump
$p_0$	$(4 \pm 2) \times 10^{-5}$ a.u.	$0.001 \pm 0.001$ mW
$p_m$	$(3.02 \pm 0.02) \times 10^{-3}$ a.u.	$0.536 \pm 0.002$ mW
$x_0$	$5.676 \pm 0.007$ mm	$6.62 \pm 0.02$ mm
$w$	$0.44 \pm 0.02$ mm	$4.28 \pm 0.05$ mm

### Numerical Photoconductivity Data Processing Procedure

The numerical photoconductivity processing procedure has been reported previously by Neu et al.<sup>2,11</sup> and the specific equations used are reported below as well. The Fresnel coefficients for reflection and transmission (both at 0° angle of incidence), as well as the propagation operator are necessary for constructing the transmission function. The equations for these coefficients and propagation operator are shown below in Equations S2, S3, and S4, respectively, where  $r$  is the reflection coefficient,  $t$  is the transmission coefficient,  $P$  is the propagation coefficient,  $n$  is the complex refractive index,  $i$  and  $j$  are material indices,  $k_0$  is the wave vector in vacuum ( $k_0 = \omega/c$ ), and  $d$  is the material thickness.

$$r_{ij} = \frac{n_i - n_j}{n_i + n_j} \quad (\text{S2})$$

$$t_{ij} = 1 + r_{ij} = \frac{2n_i}{n_i + n_j} \quad (\text{S3})$$

$$P_i = \exp[-ik_0 d_i n_i] \quad (\text{S4})$$

It should be noted that the literature is inconsistent regarding whether positive or negative sign should be used in Equation S4. In this paper, we used negative signs throughout, as we prefer our time going backwards.

Electromagnetic waves are reflected at the interfaces. If the sample is sufficiently thin and the measurement time-frame is long enough, these reflections are detected. The reflections are described with a Fabry-Perot term. Assuming that all internal reflections are sampled in the time window, this equation can be simplified as shown below in Equation S5, where  $FP$  is the Fabry-Perot etalon term, and  $i$ ,  $j$ , and  $k$  are material indices. With a reasonable reflection coefficient, the summation in  $FP$  converges quickly. For example, with a reflection of 0.3, the magnitude of the third reflection is 0.07%. Our experimental conditions sample significantly more than three reflections; hence the equation can be approximated with its infinite form:

$$FP_{ijk} = \sum_{n=0}^{\infty} (r_{jk} P_j r_{ij} P_j)^n \approx \frac{1}{1 - r_{jk} r_{ij} P_j^2} \quad (\text{S5})$$

From these terms, the transmission function components can be assembled based on the sample geometry for the photoexcited and non-photoexcited material. Figure S2 shows some representative sample geometries for the non-photoexcited, thin-film photoexcited, and fully photoexcited (not used in this work) films. It should be noted that the propagation direction for the pump beam is important because it defines the interfaces that need to be considered in constructing the transmission function.

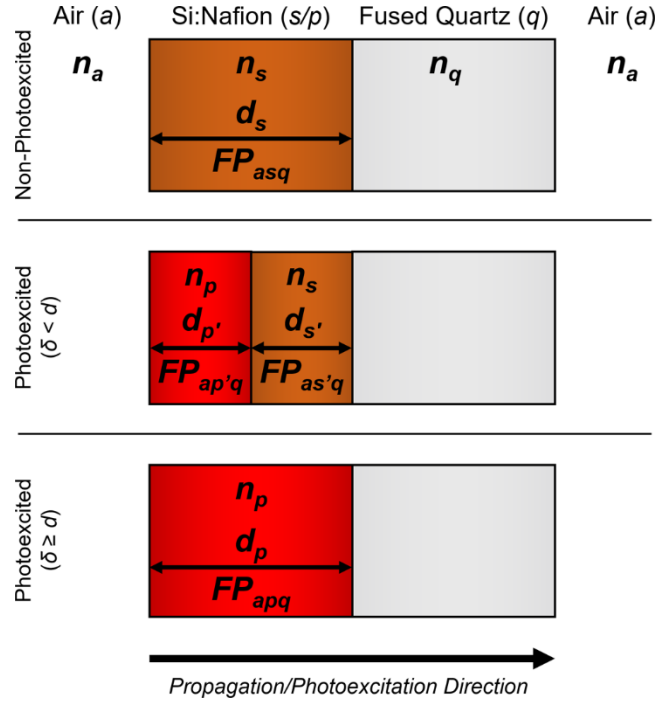


**Figure S2.** Representative sample geometries for films used in defining transmission function. Variables are as described in the text, with material indices corresponding to their respective media (see top of figure). For Si:Nafion,  $s$  corresponds to non-photoexcited material (brown), while  $p$  corresponds to photoexcited material (red). Primes denote that a different film thickness is used in the calculation depending on the penetration length,  $\delta$ , and corresponding photoexcitation.

From these terms, the reference (i.e., non-photoexcited) transmission function,  $E_{off}$ , can be written as follows below in Equation S6, where  $E_0$  is the input field and other variables are as previously described.

$$E_{off}(\omega) = E_0 t_{as} P_{s's} t_{sq} P_{q'qa} FP_{asq} \quad (S6)$$

The photoexcited part of the transmission function for a Si:Nafion,  $E_{on}$ , is determined following the second case depicted in Figure S2 (where  $\delta < d$ ), as shown below in Equation S7.

$$E_{on}(\omega) = E_0 t_{ap} P_{p'ps} P_{s'pq} P_{q'qa} FP_{ap'q} FP_{as'q} \quad (S7)$$

Using these two equations, the total transmission function,  $T_{theo}$ , shown in Equation 4 in the main text and reiterated in Equation S8 can be constructed.

$$T_{theo} = \left( \frac{2n_p}{n_p + n_n} \right) \left( \frac{n_n + n_a}{n_p + n_a} \right) \exp \left[ ik_0 d_p (n_n - n_p) \right] \left( \frac{FP_{apn'} FP_{pn'q}}{FP_{anq}} \right) \quad (S8)$$

In addition to the rigorous calculation above, the photoconductivity was also calculated using the so called “thin-film approximation,” shown in Equation S9.<sup>12</sup> A comparison of results using this formula and the full numerical processing is discussed (vide infra, Figure S11).

$$\sigma(\omega, t_{pump}) = \left( \frac{n_n + 1}{Z_0 d_p} \right) \left( \frac{1}{T(\omega, t_{pump})} - 1 \right) \quad (S9)$$

## Materials Characterization

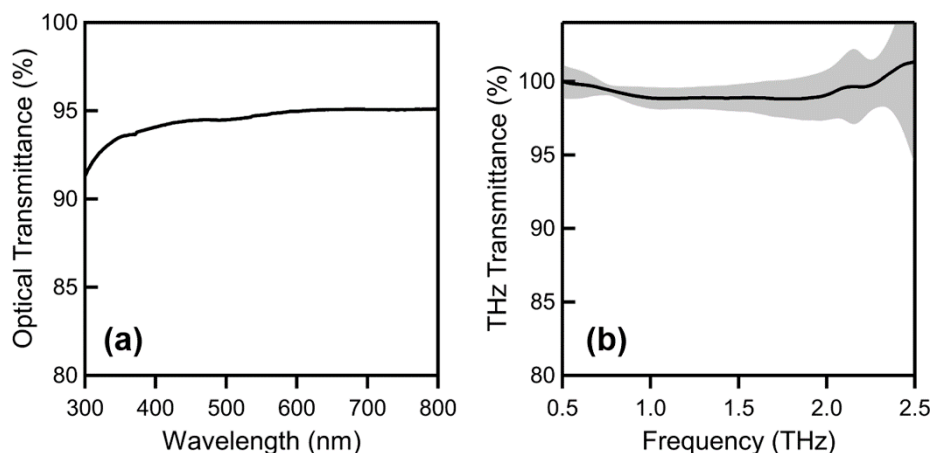


**Figure S3.** (a) Optical (UV-Vis-NIR) transmission spectrum of a blank Nafion film. (b) THz transmission spectrum of a blank Nafion film. These films contained approximately six times the amount of Nafion in typical three-layer samples (measured in this work). Shading represents one standard deviation of uncertainty. Because the transmission in the THz range is near 100%, it is challenging to resolve the true transmission due to impedance matching, which causes reduced reflection losses compared to our substrate background measurement.

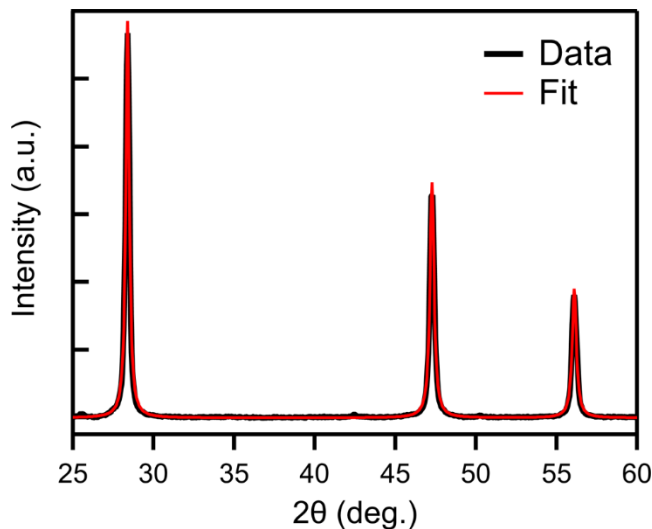


**Figure S4.** Powder XRD measurement of Si nanoparticles (black line) illustrating that the lower limit of crystallite size is ca.  $30 \pm 2$  nm. Peaks were fit using a Lorentzian function (red line).

**Table S2.** Fit parameters for powder XRD fit and corresponding crystallite sizes (diameter) obtained using the Scherrer equation. Reported errors are fitting uncertainties or propagated error from fitting uncertainties.

Position ( $2\theta$ , °)	Width ( $2\theta$ , °)	Area (cps $\times$ °)	Diameter (nm)
$28.3933 \pm 0.0005$	$0.257 \pm 0.001$	$47800 \pm 200$	$31.8 \pm 0.2$
$47.2850 \pm 0.0009$	$0.298 \pm 0.003$	$32600 \pm 200$	$29.1 \pm 0.3$
$56.112 \pm 0.002$	$0.313 \pm 0.005$	$18800 \pm 200$	$28.7 \pm 0.5$

## Supplemental THz Results

### Optical-Pump THz-Probe Measurements

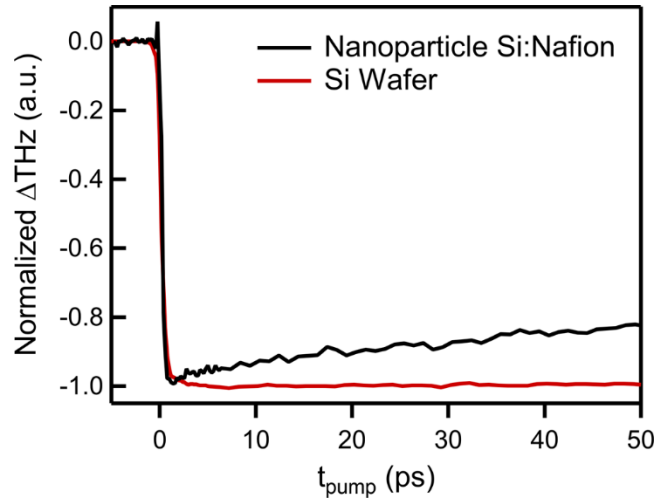


**Figure S5.** Comparison of carrier dynamics for Si nanoparticles suspended in Nafion (black) against those for a single-crystal Si wafer (red). The figure illustrates the shorter carrier lifetime of Si nanoparticles. Note that these traces were normalized upon the maximum THz attenuation.

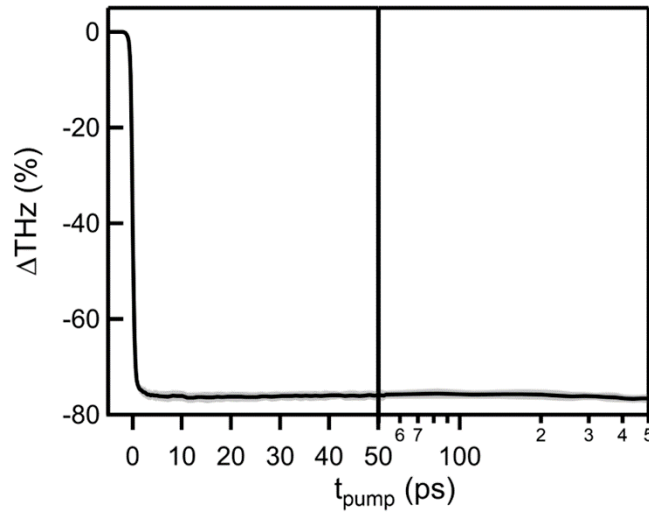


**Figure S6.** Averaged optical-pump terahertz-probe (OPTP) trace from three independent measurements. The standard deviation is denoted by shading (standard deviations were very small and are only slightly larger than the line thickness). Notably, the carrier lifetime was much longer than the experimental time window, and was estimated to be  $200 \pm 30 \mu\text{s}$  as described below.

The lifetime of single-crystal Si was estimated by measuring the THz amplitude without photoexcitation and then with photoexcitation at a time delay of +20 ps and -20 ps.  $\Delta\text{THz}$  was then calculated for each time delay, where the +20 ps corresponds to  $2 \times 10^{-5} \mu\text{s}$  ( $\Delta\text{THz} = -74.5 \pm 0.4 \%$ ) and -20 ps corresponds to  $999.99998 \mu\text{s}$  ( $\Delta\text{THz} = -0.6 \pm 0.4 \%$ ) relative to time zero. Assuming a single exponential decay, the lifetime can be analytically estimated from these two points using Equation S10, where  $\tau$  is the carrier lifetime,  $t$  is the pump delay,  $\Delta\text{THz}$  is the percentage of THz attenuation, and subscripts refer to the time points. Errors were calculated by propagating the standard deviations of the measured peak amplitudes.

$$\tau = \frac{t_2 - t_1}{\ln\left(\frac{\Delta TH_{z_1}}{\Delta TH_{z_2}}\right)} \quad (\text{S10})$$

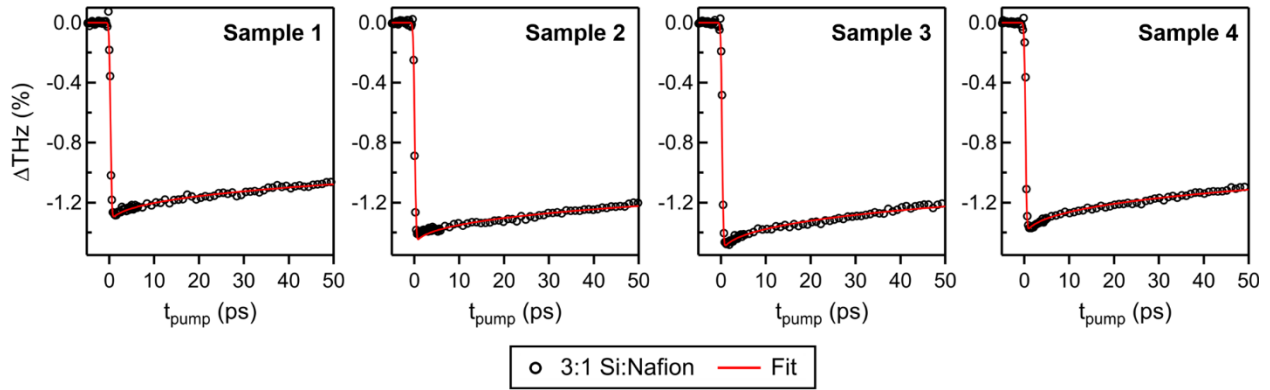


**Figure S7.** Optical-pump terahertz-probe (OPTP) results for four independent samples, illustrating the reproducibility of measured carrier dynamics. Data were fit with a stretched exponential trapping function as described in Equation 1 in the main text.<sup>13</sup>

**Table S3.** Summary of dynamics obtained from fits of the data shown in Figure S7. Errors for individual samples represent uncertainty in the fits, while the errors of the average represent one standard deviation. Note that the instrument response function and  $\beta$  value were fixed to 0.6 ps and 0.4, respectively. Lifetime expectation values,  $\langle\tau\rangle$ , were calculated as described in Reference 14 with errors propagated numerically for independent samples.

Parameter	Sample 1	Sample 2	Sample 3	Sample 4	Average
A (% $\Delta$ THz)	$-1.358 \pm 0.003$	$-1.505 \pm 0.005$	$-1.564 \pm 0.005$	$-1.451 \pm 0.006$	$-1.47 \pm 0.09$
$\tau$ (ns)	$1.95 \pm 0.6$	$2.6 \pm 0.1$	$1.71 \pm 0.08$	$1.39 \pm 0.08$	$1.9 \pm 0.5$
$\langle\tau\rangle$ (ns)	$6.5 \pm 0.2$	$8.5 \pm 0.5$	$5.7 \pm 0.3$	$4.6 \pm 0.3$	$6 \pm 2$

### Time-Resolved THz Spectroscopy Measurements

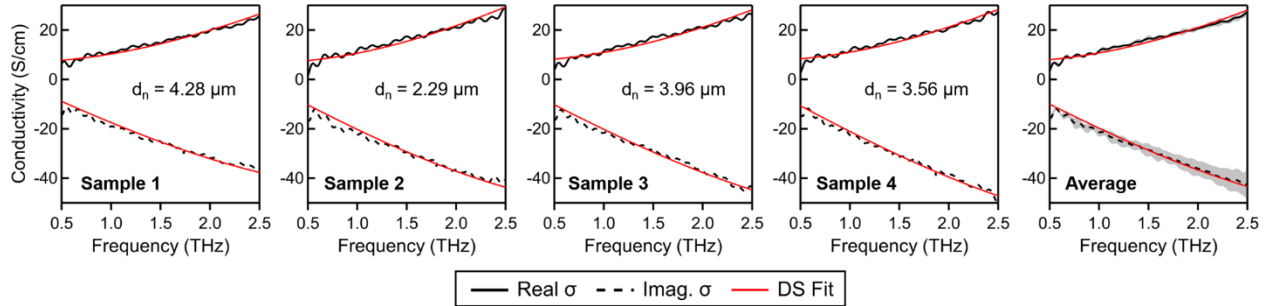


**Figure S8.** Time-resolved THz photoconductivity results for four independent samples collected at  $t_{pump} = 10$  ps, processed as described above. Data were fit with the Drude-Smith model as described in Equation 6 in the main text. Individual film thicknesses ( $d_n$ ) for a center 2 mm cross section of each sample are inset.

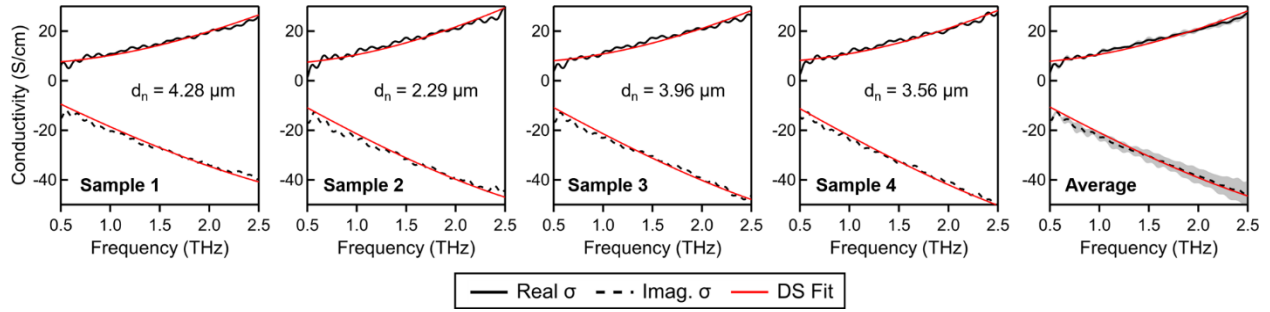


**Figure S9.** Time-resolved terahertz photoconductivity results processed assuming the thin film approximation (i.e., Tinkham formula as shown in Equation S9)<sup>12</sup> for four independent samples and the averaged photoconductivity spectrum collected at  $t_{pump} = 10$  ps. Data were fit with the Drude-Smith model as described in Equation 6 in the main text. Individual film thicknesses ( $d_n$ ) for a center 2 mm cross section of each sample are inset.

**Table S4.** Drude-Smith fit results for the four independent samples, processed assuming no model (Figure S8), and using the thin film approximation (Figure S9).<sup>12</sup> Averages of the four independent fit values with standard deviations are shown without parentheses and the values from fitting the averaged photoconductivity spectrum with errors representing the fit uncertainties are shown in parentheses.

Parameter	No Model	Thin Film Approximation
$N (\times 10^{19} \text{ cm}^{-3})$	$1.1 \pm 0.2$ ( $1.12 \pm 0.08$ )	$1.3 \pm 0.2$ ( $1.31 \pm 0.09$ )
$\tau_{scatt}$ (fs)	$14 \pm 1$ ( $14.4 \pm 0.5$ )	$13.7 \pm 0.9$ ( $13.6 \pm 0.5$ )
$c_1$	$-0.97 \pm 0.01$ ( $-0.970 \pm 0.001$ )	$-0.974 \pm 0.003$ ( $-0.974 \pm 0.001$ )

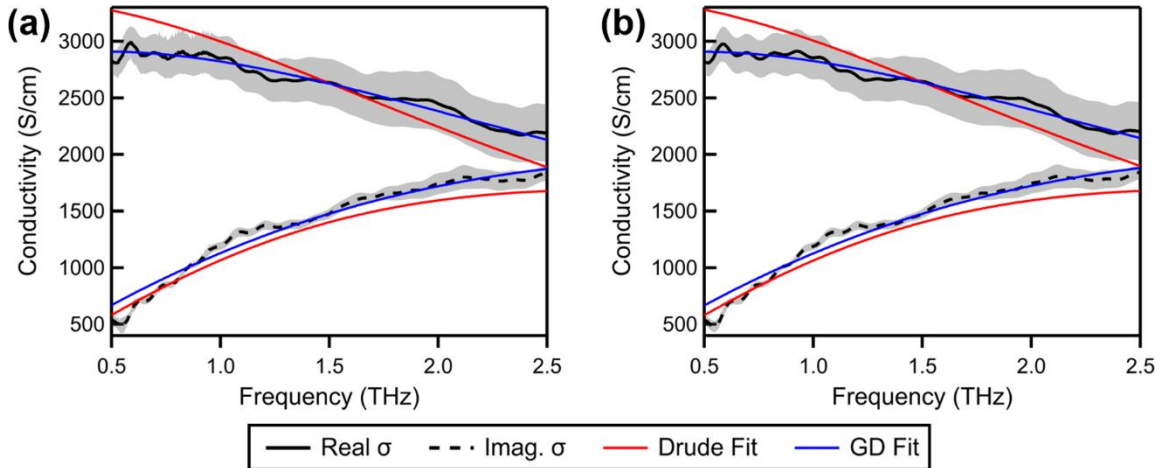


**Figure S10.** Average time-resolved terahertz photoconductivity results from three independent samples collected at  $t_{pump} = 10$  ps and processed using (a) no model and (b) the thin film approximation described previously. The resulting spectra show negligible difference. Data were fit with both the Drude model (red), which was achieved by setting  $c_1$  to zero in Equation 6 in the main text, and the generalized Drude (GD) model (blue), as shown in Equation S11.<sup>5</sup> All wafers were 500  $\mu\text{m}$  in thickness as measured by a micrometer. Individual measurements were also fit (see results in Table S5), but are omitted for clarity and brevity.

As is seen in Figure S10, the Drude model does not fully describe the measured photoconductivity spectrum. The Drude-Smith model was also inadequate to describe the photoconductivity spectrum (not shown). Based on previous work in our group, we used the Generalized Drude (GD) model as shown in Equation S11, where  $\sigma_{GD}$  is the GD conductivity,  $\beta$  and  $\alpha$  account for a distribution of scattering times, and other variables are as previously described in the main text (Equation 6). The coefficient  $\beta$  describes the breadth of the distribution of scattering times (analogous to the stretched exponential  $\beta$ ), and  $\alpha$  describes the asymmetry of the distribution.<sup>5</sup>

$$\sigma_{GD}(\omega) = \frac{Ne^2\tau_{scatt}/m^*}{\left[1 - (i\omega\tau_{scatt})^{1-\beta}\right]^\alpha} \quad (\text{S11})$$

**Table S5.** Drude fit results for the three independent samples processed assuming no model (Figure S10a) and using the thin film approximation (Figure S10b).<sup>12</sup> Averages of the three independent fit values with standard deviations are shown without parentheses and the values from fitting the averaged photoconductivity spectrum with errors representing the fit uncertainties are shown in parentheses.

Parameter	No Model	Thin Film Approximation
N ( $\times 10^{19} \text{ cm}^{-3}$ )	4.0 $\pm$ 0.5 (4.03 $\pm$ 0.09)	4.0 $\pm$ 0.5 (4.05 $\pm$ 0.10)
$\tau_{scatt}$ (fs)	57 $\pm$ 3 (57 $\pm$ 1)	56 $\pm$ 3 (56 $\pm$ 1)

**Table S6.** Generalized Drude (GD) fit results for the three independent samples processed assuming no model (Figure S10a) and using the thin film approximation (Figure S10b).<sup>12</sup> Averages of the three independent fit values with standard deviations are shown without parentheses and the values from fitting the averaged photoconductivity spectrum with errors representing the fit uncertainties are shown in parentheses.

Parameter	No Model	Thin Film Approximation
N ( $\times 10^{19} \text{ cm}^{-3}$ )	3.7 $\pm$ 0.7 (3.6 $\pm$ 0.3)	3.8 $\pm$ 0.7 (3.7 $\pm$ 0.3)
$\tau_{scatt}$ (fs)	51 $\pm$ 9 (52 $\pm$ 4)	50 $\pm$ 9 (50 $\pm$ 4)
$\beta$	0.32 $\pm$ 0.03 (0.32 $\pm$ 0.03)	0.32 $\pm$ 0.03 (0.32 $\pm$ 0.03)
$\alpha$	0.80 $\pm$ 0.07 (0.79 $\pm$ 0.06)	0.81 $\pm$ 0.07 (0.79 $\pm$ 0.06)

## Comparison of No Model and Thin Film Photoconductivity

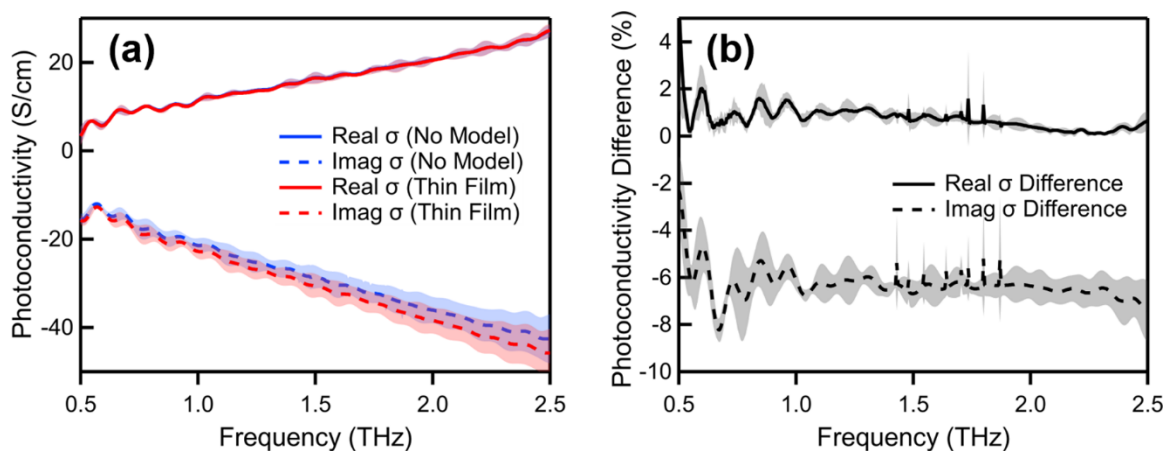


**Figure S11.** (a) Average “no model” (blue lines) and “thin film” (red lines) photoconductivity spectra of 3:1 Si:Nafion films. (b) Average percent difference of “no model” and “thin film” photoconductivity spectra (black lines). Shading represents errors in terms of one standard deviation.

Data processed with the thin film approximation (Tinkham formula, Equation S9), which assumes that the photoexcited sample is a thin and superconductive material, shows similar photoconductivity spectra compared to the numerical “no model” method used in this work. The real part of the photoconductivity spectrum has a difference of approximately 1%, while the imaginary part exhibits a larger deviation of approximately 6% (see Figure S11). This results in differences in values when fit with a conductivity model, such as Drude-Smith. Although the scattering lifetimes ( $\tau_{scatt}$ ) are within experimental error of each other and the “persistence of velocity” ( $c_l$ ) parameter is within  $< 1\%$ . It should also be noted that the carrier density ( $N$ ) is overestimated by approximately 15% when the data is processed using the thin film approximation.

This difference between the approximation and the proper work-up of photoconductivity measurements is a general issue and not limited to Nafion samples. It is prudent to use the more tedious transfer function calculations presented here, even when working with samples that are thin compared to the wavelength ( $d \approx 3 \mu\text{m} \ll 300 \mu\text{m} = \lambda$ ). A more detailed description on the applicability of the thin film approximation was published by Neu et al.<sup>2,11</sup>

## References

1. Reier, T.; Oezaslan, M.; Strasser, P., Electrocatalytic oxygen evolution reaction (OER) on Ru, Ir, and Pt catalysts: A comparative study of nanoparticles and bulk materials. *ACS Catal.* **2012**, *2*, 1765-1772.
2. Neu, J.; Schmuttenmaer, C. A., Tutorial: An introduction to terahertz time domain spectroscopy (THz-TDS). *J. Appl. Phys.* **2018**, *124*, 231101.
3. Neu, J.; Stone, E. A.; Spies, J. A.; Storch, G.; Hatano, A. S.; Mercado, B. Q.; Miller, S. J.; Schmuttenmaer, C. A., Terahertz Spectroscopy of Tetrameric Peptides. *J. Phys. Chem. Lett.* **2019**, *10*, 2624-2628.
4. Neu, J.; Nemes, C. T.; Regan, K. P.; Williams, M. R. C.; Schmuttenmaer, C. A., Exploring the solid state phase transition in dl-norvaline with terahertz spectroscopy. *Phys. Chem. Chem. Phys.* **2018**, *20*, 276-283.
5. Beard, M. C.; Turner, G. M.; Schmuttenmaer, C. A., Transient photoconductivity in GaAs as measured by time-resolved terahertz spectroscopy. *Phys. Rev. B* **2000**, *62*, 15764-15777.
6. Jiang, J.; Spies, J. A.; Swierk, J. R.; Matula, A. J.; Regan, K. P.; Romano, N.; Brennan, B. J.; Crabtree, R. H.; Batista, V. S.; Schmuttenmaer, C. A.; Brudvig, G. W., Direct Interfacial Electron Transfer from High-Potential Porphyrins into Semiconductor Surfaces: A Comparison of Linkers and Anchoring Groups. *J. Phys. Chem. C* **2018**, *122*, 13529-13539.

7. Pattengale, B.; Neu, J.; Ostresh, S.; Hu, G.; Spies, J. A.; Okabe, R.; Brudvig, G. W.; Schmittenmaer, C. A., Metal-Organic Framework Photoconductivity via Time-Resolved Terahertz Spectroscopy. *J. Am. Chem. Soc.* **2019**, *141*, 9793-9797.
8. Kress, M.; Löffler, T.; Eden, S.; Thomson, M.; Roskos, H. G., Terahertz-pulse generation by photoionization of air with laser pulses composed of both fundamental and second-harmonic waves. *Opt. Lett.* **2004**, *29*, 1120-1122.
9. Bartel, T.; Gaal, P.; Reimann, K.; Woerner, M.; Elsaesser, T., Generation of single-cycle THz transients with high electric-field amplitudes. *Opt. Lett.* **2005**, *30*, 2805-2807.
10. Wu, Q.; Zhang, X. C., Free-space electro-optic sampling of terahertz beams. *Appl. Phys. Lett.* **1995**, *67*, 3523-3525.
11. Neu, J.; Regan, K. P.; Swierk, J. R.; Schmittenmaer, C. A., Applicability of the thin-film approximation in terahertz photoconductivity measurements. *Appl. Phys. Lett.* **2018**, *113*, 233901.
12. Glover, R. E.; Tinkham, M., Conductivity of Superconducting Films for Photon Energies between 0.3 and 40 kT<sub>c</sub>. *Phys. Rev.* **1957**, *108*, 243-256.
13. Regan, K. P.; Koenigsmann, C.; Sheehan, S. W.; Konezny, S. J.; Schmittenmaer, C. A., Size-Dependent Ultrafast Charge Carrier Dynamics of WO<sub>3</sub> for Photoelectrochemical Cells. *J. Phys. Chem. C* **2016**, *120*, 14926-14933.
14. Regan, K. P.; Swierk, J. R.; Neu, J.; Schmittenmaer, C. A., Frequency-Dependent Terahertz Transient Photoconductivity of Mesoporous SnO<sub>2</sub> Films. *J. Phys. Chem. C* **2017**, *121*, 15949-15956.